machines

MDPI

Article

Analysis of Performance and Noise on an Asymmetric Double-Suction Fan with Non-Uniformity Inlet Conditions

Yougen Huang [1], Bin Li [2], Haohui Chen [2], Weigang Yang [2], Qianhao Xiao [3,4] and Jun Wang [1,*]

[1] School of Energy and Power Engineering, Huazhong University of Science and Technology, Wuhan 430074, China; huangyga@hust.edu.cn
[2] Ningbo Fotile Kitchenware Co., Ltd., Ningbo 315336, China
[3] School of Energy and Power Engineering, Changsha University of Science and Technology, Changsha 410205, China
[4] Key Laboratory of Renewable Energy Electric-Technology of Hunan Province, School of Energy and Power Engineering, Changsha University of Science and Technology, Changsha 410114, China
* Correspondence: wangjhust@hust.edu.cn

Abstract: Asymmetric double-suction centrifugal fans are commonly employed in home kitchens to remove cooking pollutants, and their performance is critical to maintaining a healthy indoor environment. However, inlet condition variations significantly influence the aerodynamic efficiency and noise levels. This study utilizes a combination of performance testing and a large eddy simulation to analyze the impact of different inlet conditions on the performance curve, impeller outlet pressure pulsation, unsteady flow structures, and sound quality of an asymmetric double-suction centrifugal fan. A non-uniform air distribution at the inlet is proposed to enhance the fan's aerodynamic and noise characteristics. The findings reveal that when the inlet area is reduced to less than 70% of its fully open state, the aerodynamic performance declines with decreasing intake area. The amplitude of the superimposed blade-passing frequency is minimized when only the left inlet is open; the pressure coefficient's fluctuation amplitude in the time domain reaches 0.4, with sharpness peaking at 3.1. In the optimized design, the maximum deviation in total pressure efficiency is limited to 1.96%, with loudness reduced by four sones and improved sharpness and roughness. These results provide valuable insights into the design and noise reduction of asymmetric double-suction squirrel-cage fans.

Keywords: inlet condition; large eddy simulation; vortex structure; pressure pulsation; acoustic quality characteristics

check for updates

Academic Editors: Massimiliano De Agostinis and Ciro Santus

Received: 25 March 2025
Revised: 13 May 2025
Accepted: 21 May 2025
Published: 27 May 2025

Citation: Huang, Y.; Li, B.; Chen, H.; Yang, W.; Xiao, Q.; Wang, J. Analysis of Performance and Noise on an Asymmetric Double-Suction Fan with Non-Uniformity Inlet Conditions. *Machines* **2025**, *13*, 463. https://doi.org/10.3390/machines13060463

Copyright: © 2025 by the authors. Licensee MDPI, Basel, Switzerland. This article is an open access article distributed under the terms and conditions of the Creative Commons Attribution (CC BY) license (https://creativecommons.org/licenses/by/4.0/).

1. Introduction

Squirrel-cage fans are widely used in ventilation, fire protection, and smoke exhaust fields due to their high flow rate and low noise [1,2]. These fans are the core power of range hoods, mainly used to remove the fumes generated during cooking. They are also an important source of noise in home environments and will impact human health [3,4]. During the actual operation of the range hood, the inlet conditions and structure will be dynamically adjusted according to the working status of the stoves on both sides below to improve the capture efficiency, forming different intake conditions, which can bring about non-uniform inflow, thereby affecting the aerodynamic performance, internal unsteady flow, and noise of the fan [5–7]. On the other hand, under the influence of the motor's structure and space size limitations, the flow separation inside the double-suction squirrel-cage fan is further increased [8–11].

Currently, research methods for analyzing the internal pressure pulsation characteristics of fans include numerical simulations, experimental studies, and theoretical approaches. Kirchhofer et al. [12] conducted a comparative study using different turbulence models (S-A, k-ε, and SST k-ω) to simulate the flow field within a fan and compared these results with particle image velocimetry measurements. Their findings showed that the SST k-ω model provided the most accurate predictions for the characteristic curves and internal velocity fields. Similarly, Yang et al. [13] demonstrated that the SST model offers the lowest error in performance predictions when simulating a range hood equipped with a squirrel-cage fan.

The known literature indicates that the pressure and its fluctuations are highly consistent with the noise characteristics of the fan. It is feasible to study the pressure pulsation characteristics inside the fan to reflect the noise characteristics of the fan. Ballesteros-Tajadura et al. [14], Li et al. [15], and Xu et al. [16] all used numerical simulation methods to obtain the pressure pulsation inside the fan impeller, and the numerical calculation results matched well with experimental values. Zhang et al. [17] calculated the three-dimensional unsteady flow and acoustic field of the fan via direct computational aeroacoustics based on the lattice Boltzmann method. Experimental data from the performance test bench and the semi-anechoic chamber were used to validate the accuracy of the numerical simulation results. Min et al. [18] used URANS and FFT to analyze the interaction between the rotors of a centrifugal fan and its impact on acoustic performance. Zhang et al. [19] proposed an experimentally based vibration noise optimization control method for a particular centrifugal fan, leading to a 6.23 dB reduction. Xiao et al. [20] introduced a new empirical noise model to more accurately predict fan noise. Velarde-Su'arez et al. [21,22] found a significant circumferential asymmetry in the magnitude and direction of the velocity of a squirrel-cage fan. Oro et al. [23–25] presented a numerical methodology to evaluate the flow unsteadiness and impeller-tongue interaction. Kato [26] captured the large eddies in the flow and found that the large eddies were the primary noise source. Liu et al. [27], using large eddy simulation and acoustic analogy theory, analyzed the flow noise at a natural gas transmission and distribution station. A small hole muffler was designed to effectively reduce low-frequency noise by up to 37.4 dB, with an average noise reduction of approximately 20.9 dB. Deng et al. [28–30] mentioned more efficient and advanced CFD tools that could improve the LES results.

In the study of internal flow characteristics and optimization improvements for double-suction squirrel-cage fans, the primary areas of focus include flow deflectors, blade profiles, and volute designs. Gholamian et al. [31] studied the impact of four inlet nozzle sizes on fan performance and found that the inlet nozzle size and the impeller inner diameter are crucial for fan efficiency. Huang et al. [32] found that range hood noise predominantly consists of discrete low-frequency components, with most of the noise being transmitted through the inlet. Lv et al. [33] demonstrated that biomimetic volutes can significantly enhance aerodynamic performance under rated conditions. Lei et al. [34] showed that installing flow straighteners can notably reduce vortex intensity. Liu et al. [35] introduced a non-axisymmetric D-type inlet nozzle to mitigate severe backflow development at the volute tongue. Jiang et al. [36] explored a random modulation method to reduce tonal noise and reshape the noise spectrum. Xiao et al. [37] optimized the blade shape of the squirrel-cage fan within a range hood using a surrogate model, resulting in a 2.9% increase in maximum volume flow rate in the optimal design. In recent years, several scholars [38–42] have developed optimization design methods to enhance the aerodynamic performance and reduce the noise of centrifugal fans, achieving positive results in engineering applications.

In conclusion, the noise sources within squirrel-cage fans are intricate, primarily stemming from complex, unsteady flows. However, existing research predominantly addresses uniform air intake, fan placement within equipment, and steady-state simulations. These

approaches fall short in examining the internal flow dynamics and noise distribution characteristics of asymmetric double-suction squirrel-cage fans under non-uniform air intake conditions. There is a significant gap in understanding noise quality. The present study employs large eddy simulation (LES) numerical methods to analyze the internal flow of asymmetric double-suction centrifugal fans integrated within complete equipment. It investigates the impact of varying air intake conditions on impeller outlet pressure pulsation, internal complex flow patterns, and noise characteristics at the operator position. This research aims to offer valuable insights and a solid theoretical foundation for optimizing the design of dual-suction centrifugal fans.

This study introduces a non-equal flow inlet scheme, derived from unsteady simulation analysis and noise testing, that enhances the aerodynamic performance and reduces noise in asymmetric double-suction centrifugal fans. While this approach offers significant engineering guidance, further research is necessary. Future work should include integrating kitchen space considerations, performing multi-phase flow coupling analysis, accounting for human behavior and smoke exhaust conditions, accumulating measurement data, and developing a reduced-order analysis model for inlet parameters, aerodynamic noise, and air pollution concentration. Additionally, establishing a multi-objective optimization model for air quality and kitchen noise levels, dynamically optimizing inlet conditions, and ensuring superior performance of squirrel-cage fans across various operating scenarios will be essential.

2. Aerodynamic Performance Analysis

2.1. Fan Model

This study focuses on an asymmetric double-suction squirrel-cage fan used in range hoods. Figure 1a illustrates the internal structure of the device, where the test fan is mounted in the upper fan frame. The square intake chamber is divided into two paths by the double-suction fan: the front and rear. The front path is associated with the narrow blade side, while the rear path corresponds to the wider impeller side. Airflow is drawn from a narrow, tapered duct below, passing through the front and rear intake chambers before entering the fan via the respective intake nozzles. A motor and its support structure are located in the narrow impeller channel, and these elements, along with the dimensions of the intake chambers and airflow conditions on both sides of the range hood, create asymmetric intake conditions. Consequently, the flow field analysis in the subsequent sections primarily compares the flow structures between the wide and narrow impellers corresponding to the front and rear paths.

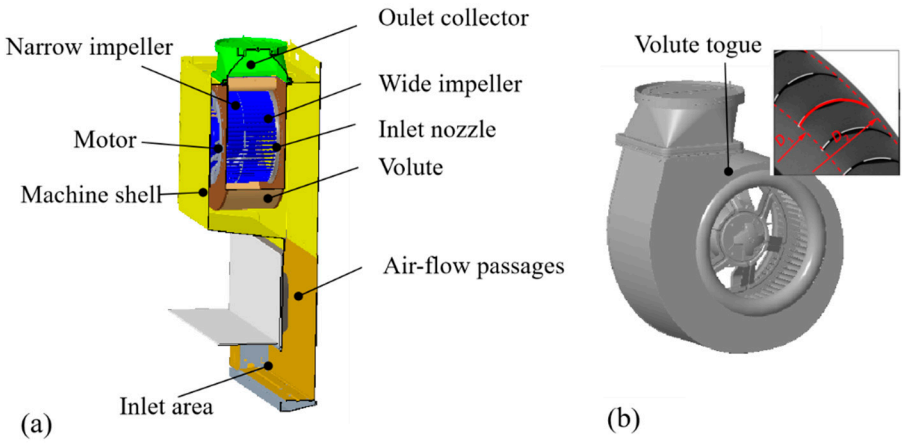


Figure 1. Schematic of the test range hood: (**a**) entire machine; (**b**) squirrel-cage fan.

The critical parameters of the test fan are illustrated in Figure 1b, with the specific values provided in Table 1. The rotor inner and outer diameters are 210 mm and 254 mm, respectively. The blade design features a single circular arc structure, with inlet and outlet angles of 105° and 167°. The impeller widths are 128 mm on the wide side and 50 mm on the narrow side. In this study, a fan speed of 1200 rpm and a flow rate of 12 m^3/min were chosen based on typical operating conditions for residential kitchen range hoods. These parameters represent common usage scenarios, ensuring that the results are applicable to real-world situations. These parameters represent common usage scenarios, ensuring that the results are applicable to real-world situations.

Table 1. Design parameters of a double-suction centrifugal fan.

Parameter	Value
Impeller inlet diameter	209 mm
Impeller outlet diameter	232 mm
Impeller width	128 mm/50 mm
Blade inlet angle	105°
Blade outlet angle	167°
Volume flow rate	12 m^3/min

2.2. Test Device

The aerodynamic performance testing apparatus is based on the Chinese range hood measurement standard GB/T 17713 [43]. The experimental setup in Figure 2 has a flow measurement range of 0–35 m^3/min. Local atmospheric pressure, temperature, and humidity are recorded using an environmental temperature and humidity sensor and input into the aerodynamic performance measurement software, with temperature measurement errors of ±0.5 °C and humidity measurement accuracy of 1%. An air conditioning system in the laboratory maintains the experimental environment at around 20 °C and 85% relative humidity. The motor current is controlled via different settings on the electronic control panel to adjust the fan speed displayed on the control panel. Various nozzle combinations are used to simulate different fan operating conditions.

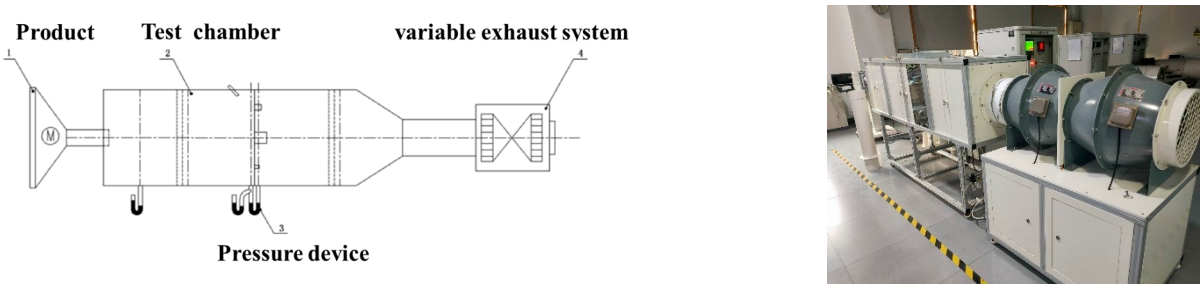


Figure 2. The aerodynamic performance testing device.

2.3. Analysis of Aerodynamic Performance

Given the variation in cooking habits, long-term use of range hoods can lead to oil accumulation, potentially causing blockages in the inlet structure. On the other hand, dynamically adjusting the inlet conditions and structure according to the working state of the stoves on both sides below becomes a scheme to improve the effect of cooking fume absorption. Additionally, the rotational direction of the impeller may result in uneven inlet flow fields. To address these issues, nine specific inlet conditions have been defined, as illustrated in Figure 3.

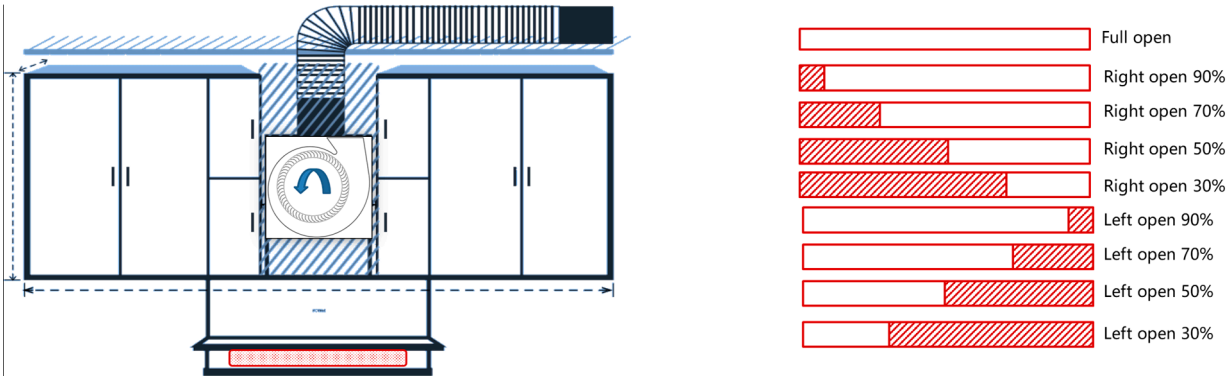


Figure 3. Nine inlet conditions with considering the direction of rotation.

The data are derived from aerodynamic performance tests. To ensure accuracy, we compared measurements taken at different times and with various fan products, maintaining a deviation in air volume measurement of no more than 1%. Data were collected while testing nine different inlet conditions at a constant fan speed. For each condition, we gathered 13 sets of data on air volume, static pressure, total pressure, and power by adjusting the nozzles. Using this information, we calculated the total pressure efficiency. The experimental results presented in Figure 4 demonstrate that the size of the range hood's air inlet area has a substantial impact on its aerodynamic performance. Interestingly, the fan's performance is better when the inlet is 90% open on both sides compared to when it is fully open. This improvement is likely due to excessive airflow velocity changes from the range hood's inlet to the fan's inlet, which leads to flow loss. However, when the inlet area is reduced to less than 70% of the fully open condition, the aerodynamic performance declines as the inlet area decreases. Additionally, at 30% left and right openings, a noticeable difference in aerodynamic performance is observed, suggesting that the optimal inlet area is asymmetrical between the left and right sides.

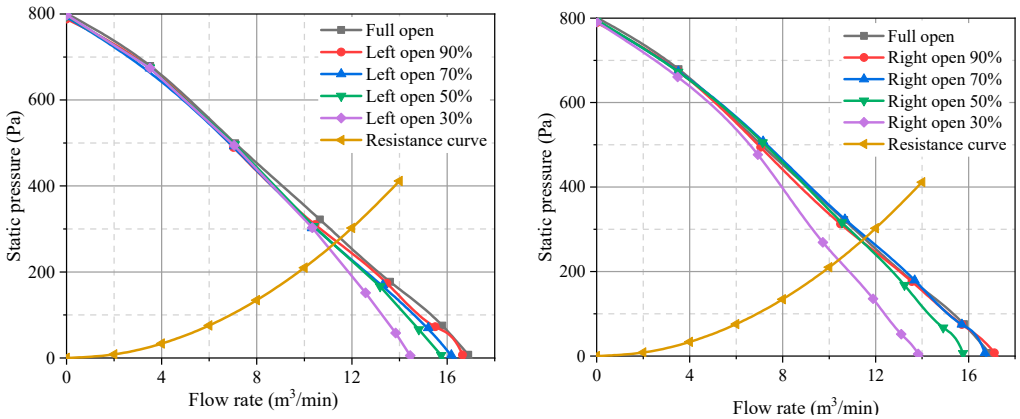


Figure 4. Aerodynamic performance of nine inlet conditions.

Figure 5 illustrates the maximum total pressure efficiency for the nine different inlet conditions, revealing distinct patterns between the left and right inlet areas. The highest efficiency occurs under fully open and 90% right opening conditions. Conversely, the maximum total pressure efficiency drops significantly when the right inlet is only 30% open. This suggests that as the left opening area decreases, the resistance in the air duct increases in a nonlinear manner, while the left side shows a linear decrease in efficiency.

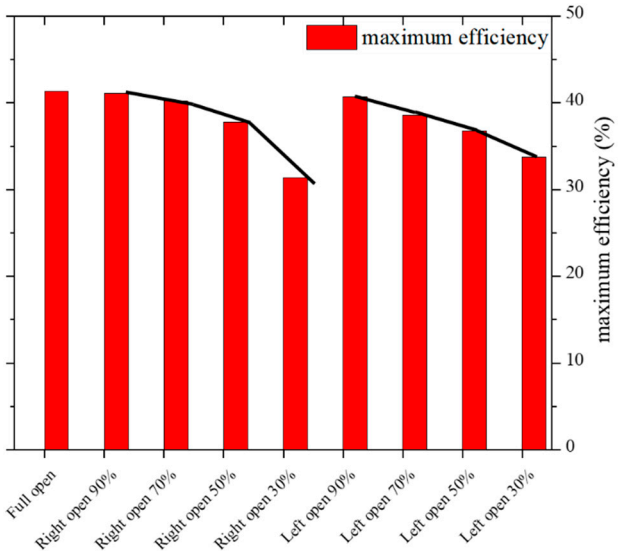


Figure 5. Maximum efficiency of nine inlet conditions.

3. Analysis of Internal Flow Characteristics

3.1. Numerical Method

The kitchen model in this paper represents a typical household kitchen layout, as shown in Figure 6, with overall kitchen dimensions of 3.6 m × 2.1 m × 2.1 m. There are 60 blades in the impeller, consisting of a wide and narrow impeller, forming a double-suction structure. Moreover, a 1200 rpm speed resulted in a blade-passing frequency of 1200 Hz and a shaft frequency of 20 Hz. Other parameters are listed in Table 1. The entire computational domain is meshed using ANSYS ICEM 2022R1, with hexahedral mesh division for the impeller and refinement of the impeller blade wall mesh shown in Figure 7, ensuring a rotational domain with $y^+ \leq 1$. The remaining areas are meshed using tetrahedral elements.

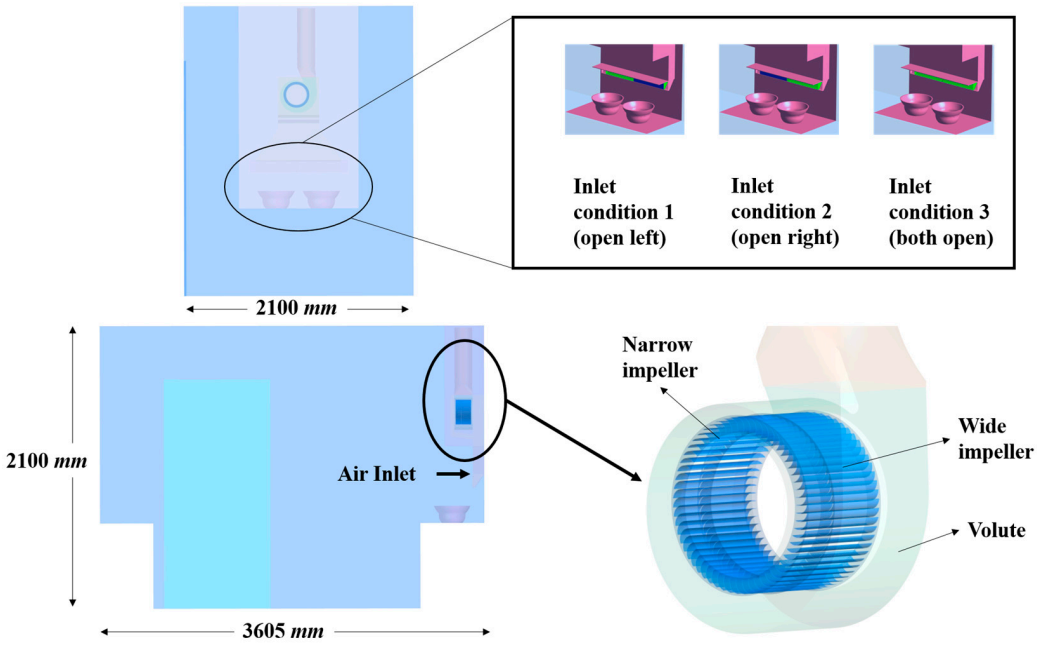


Figure 6. Three-dimensional layout.

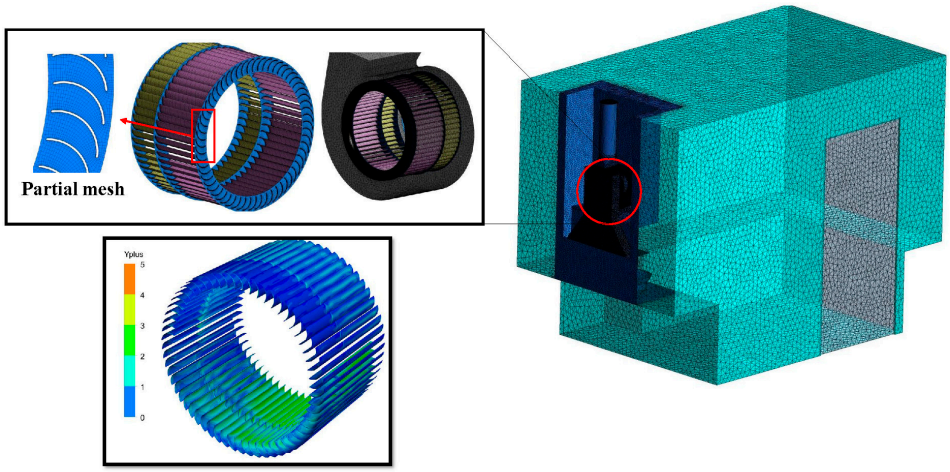


Figure 7. Schematic diagram of the grid.

Based on the aerodynamic performance analysis in the previous text, an internal flow study was conducted on the inlet conditions of 50% left opening, 50% right opening, and full opening. These conditions were named inlet condition 1, inlet condition 2, and inlet condition 3, respectively, to further analyze the internal mechanism for the performance differences.

At the rated operating conditions, the LES was employed to numerically simulate seven different mesh partitioning schemes. This turbulence model can derive the LES governing equations by adding a filtering function to the Navier–Stokes equations.

$$\frac{\partial \overline{u_i}}{\partial t} + \frac{\partial}{\partial x_j}\left(\overline{u_i u_j}\right) = -\frac{1}{\rho}\frac{\partial \overline{p}}{\partial x_i} + \frac{\partial}{\partial x_j}\left[\nu\left(\frac{\partial \overline{u_i}}{\partial x_j} + \frac{\partial \overline{u_j}}{\partial x_i}\right)\right] + \frac{\partial \overline{\tau_{ij}}}{\partial x_j} + S_i \tag{1}$$

$\overline{\tau_{ij}}$ is the subgrid-scale stress, abbreviated as SGS stress, expressed as:

$$\overline{\tau_{ij}} = \overline{u_i u_j} - \overline{u_i}\,\overline{u_j} \tag{2}$$

The most commonly used subgrid-scale model is the Smagorinsky–Lilly model.

$$\overline{\tau_{ij}} - \frac{1}{3}\delta_{ij}\overline{\tau_{kk}} = -2v_T\overline{S_{ij}} \tag{3}$$

$\overline{S_{ij}}$ is the strain tensor, v_T is the subgrid-scale turbulent viscosity.

$$v_T = (C_s\Delta)^2\left|\overline{S}\right| \tag{4}$$

$$\left|\overline{S}\right| = \sqrt{2\overline{S_{ij}S_{ij}}} \tag{5}$$

Δ is the filter width, C_s is the Smagorinsky–Lilly constant, take $C_s = 0.1$.

The computational domain was evaluated based on whether the total fan pressure stabilized as the grid number increased to verify mesh independence. When the grid number exceeded 9.18×10^6 under consistent computational conditions, changes in the total fan pressure became negligible. A grid total of 9.18×10^6 was selected for the numerical simulation to balance computational efficiency and accuracy. The mesh configuration is illustrated in Figure 8.

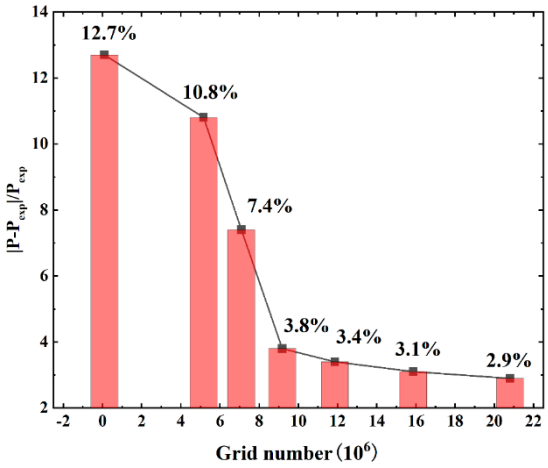


Figure 8. Relative error with grid number.

Steady-state simulations were conducted using the SST k-ω turbulence model, chosen for its comprehensive accuracy as the optimal eddy-viscosity model. The entire computational process was carried out in ANSYS Fluent. The inlet boundary condition was defined as a pressure inlet, while the outlet was set as a mass flow outlet with a flow rate of 12 m^3/min. Interfaces were applied at the boundaries between different regions to enable efficient data transfer.

The steady-state results are used as initial values for unsteady simulations. The sliding mesh model facilitates data transfer at the dynamic–static interface. The numerical calculations are set to rotate the impeller by 0.5 degrees per step, with a corresponding time step of 6.9444×10^{-5} s. Moreover, a comparison of the pressure curves obtained from the experiment and CFD calculation is shown in Figure 9. The results from both the simulation and experiments show a strong correspondence in the high flow rate region. In the low flow rate area, the trends of both results are generally consistent, with the maximum error kept within 3%.

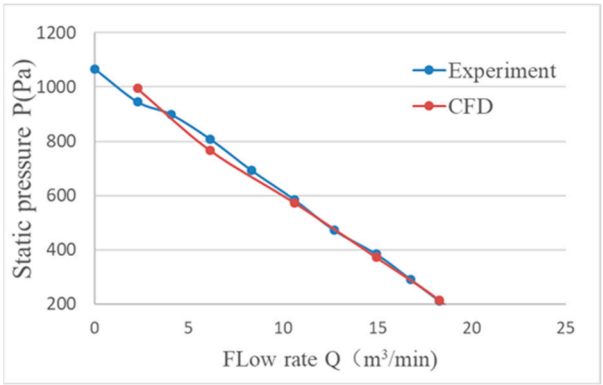
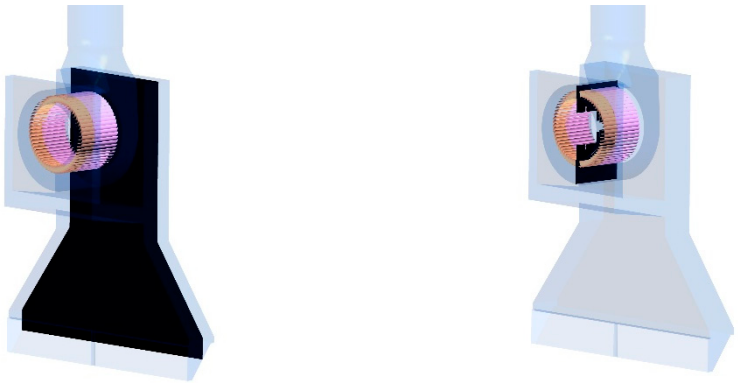


Figure 9. Comparison of experiment and CFD calculation.

3.2. Flow Field Analysis

In the overall streamlined analysis (Figure 10), inlet condition 3 demonstrates lower velocities and more uniform streamlines at the fan inlet compared to inlet conditions 1 and 2. The figure reveals that fluid entering the fan inlet does not do so uniformly, which is a critical factor to consider in numerical simulations when modeling the kitchen environment. To examine the flow state near the impeller, two planes (Planes 1 and 2) were created. Figure 11 shows that while the flow under inlet condition 3 is relatively uniform, there is a distinct low-speed zone in the middle area. Under inlet conditions 1 and 2, the velocity

distribution within the intake chamber is uneven, with large low-speed zones in non-intake regions and increased vortex separation. Given the impeller rotation direction, airflow under inlet condition 1 enters from the left side, affecting the impeller's rotation direction.



(**a**) Plane 1 (**b**) Plane 2

Figure 10. Slice schematic diagram.

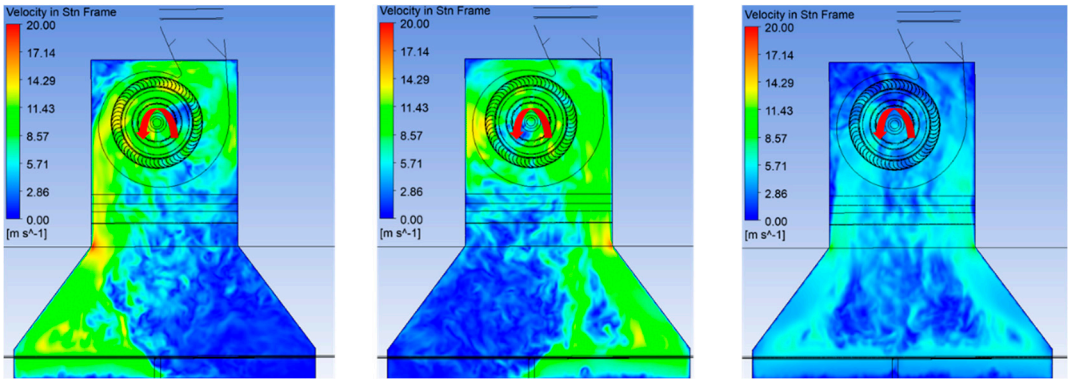


Figure 11. Vorticity and streamline distribution (Plane 1).

Figure 12 further illustrates that asymmetric inlet conditions generate large-scale circulation in another dimension, directly caused by the impeller's uneven air intake. From the perspective of plane 1, where the impeller rotates counterclockwise, inlet condition 1 shows that flow entering from the left side opposes the impeller's rotation, resulting in higher impact forces on the fluid and more complex flow characteristics. In contrast, inlet condition 2, where flow enters from the right side, aligns with the impeller's rotation direction, leading to a more stable internal flow state compared to condition 1.

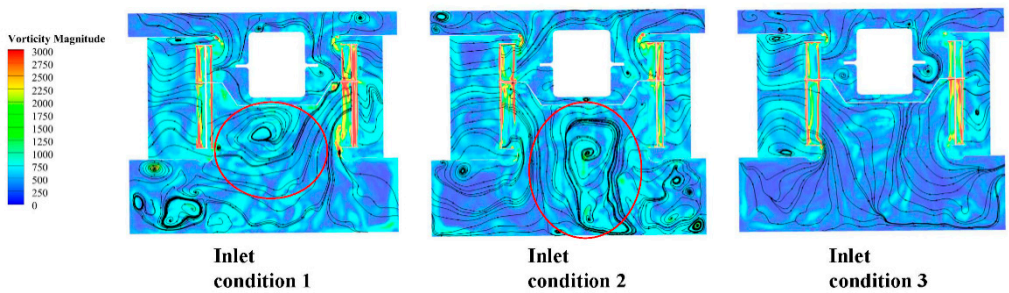


Figure 12. Vorticity and streamline distribution (Plane 2).

3.3. Influence of Inlet Conditions on the Pressure Fluctuation of Impeller Outlet

The arrangement of all pressure fluctuation measurement points in this study is shown in Figure 13. Eight monitoring points (C1~C8, D1~D8) are uniformly arranged around the

outlet of the wide and narrow impellers. Pressure fluctuations data within a certain period are dimensionless processed, defining the pressure coefficient C_p and the root mean square of pressure fluctuation coefficient C_p-RMS:

$$C_p = \frac{p - \overline{p}}{0.5\rho u_2^2} \tag{6}$$

$$C_p - RMS = \sqrt{\frac{\sum_{i=1}^{n} \left(C_{pi} - \overline{C}_p\right)^2}{n}} \tag{7}$$

where p is the instantaneous pressure value. $\overline{p}$ is the mean value of pressure data in a specific time period. u_2 is the circumferential velocity of the impeller outlet. n is the number of selected pressure coefficient samples.

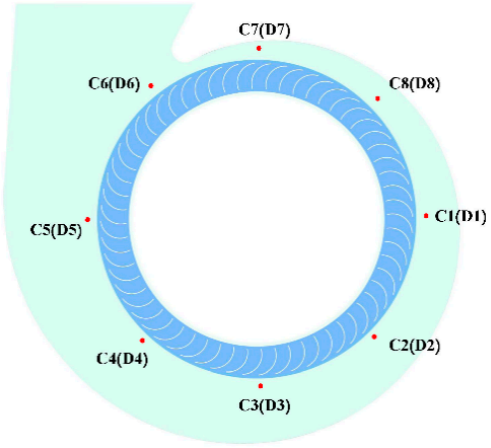


Figure 13. Location distribution of monitoring points.

The computational results indicate that the impact of different inlet conditions on the time domain is generally similar. Time-domain analysis offers a detailed description of the instantaneous characteristics of pressure signals, while frequency-domain analysis provides a deeper understanding of the frequency components and their sources. By combining both approaches, we gain a more comprehensive understanding of the fan's flow field characteristics and their relationship with noise and vibration. As shown in Figure 14, inlet condition 3 provides more stable time-domain characteristics, with a higher mean pressure coefficient (C_p), suggesting that the fluid gains more energy under this condition. Figure 15 illustrates that under inlet condition 1, the pressure signals at various monitoring points exhibit a distinct peak–valley pattern over time. This pattern is due to the periodic impact of the blades on the surrounding air as the impeller rotates, with each cycle producing 60 distinct peaks corresponding to the number of blades. Notably, under inlet condition 1, there are significant fluctuations in the C_p near the C1 measurement point for the wide impeller and near the D5 measurement point for the narrow impeller. The time-domain characteristics for the wide impeller are comparatively more stable, with a maximum C_p pulsation amplitude of 0.25, while the narrow impeller experiences a higher amplitude of 0.4. Subsequent analysis will focus on the flow characteristics near the C1 measurement point for the wide impeller and the D5 measurement point for the narrow impeller under inlet condition 1.

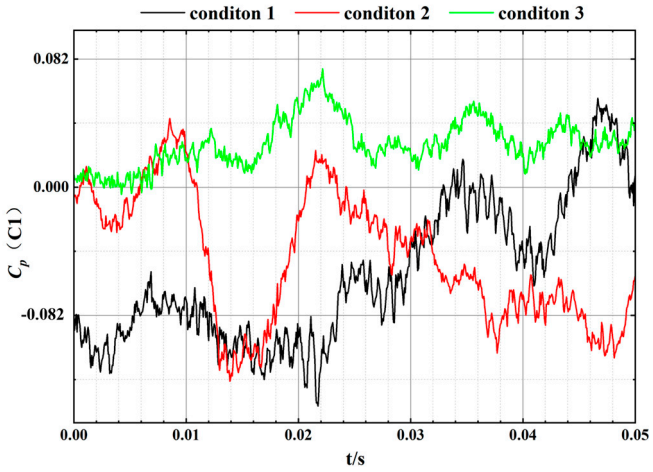


Figure 14. Time-domain characteristics of C1 measuring point under different inlet conditions.

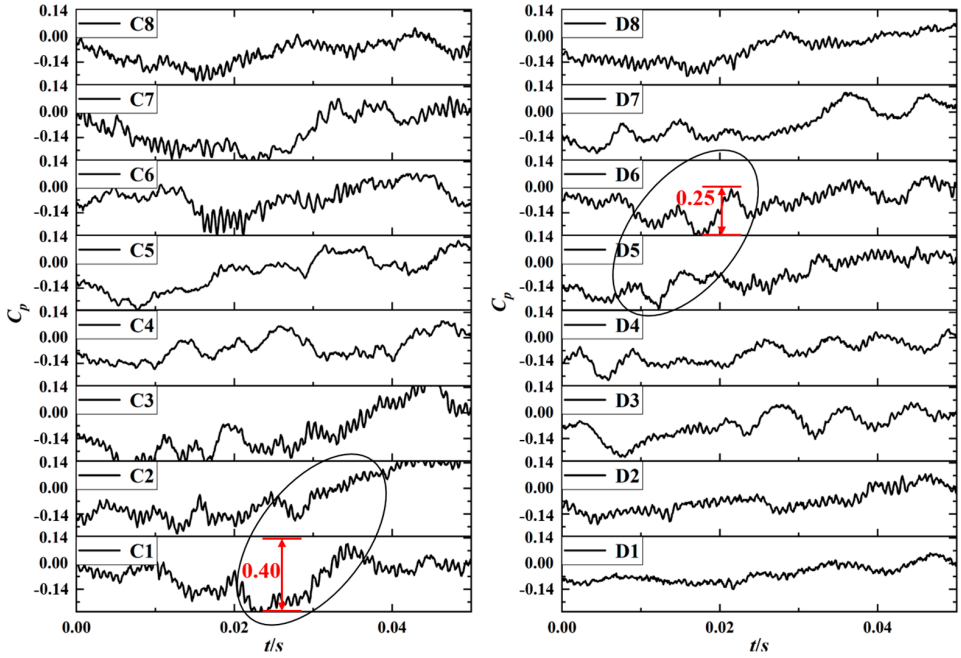


Figure 15. Time-domain characteristics of impeller outlet measuring points (inlet condition 1).

The rotor–stator interaction at the impeller outlet serves as the main source of internal unsteady pulsations in the fan. To capture the pulsation characteristics in this region and assess the impact of different inlet conditions on the rotor–stator interaction, eight monitoring points (C1~C8 and D1~D8) are evenly distributed at the outlet of each impeller. The time-domain signals from these points are processed using Fast Fourier Transform (FFT) with a Hanning window to analyze the frequency-domain signals under various inlet conditions.

Figure 16 illustrates the pressure pulsation frequency spectrum at the outlet under inlet condition 1. The central peak values of pressure pulsations at different monitoring points are all observed at the blade-passing frequency (f_{BPF}), though the amplitude varies significantly. Under inlet condition 1, a broad-frequency signal is evident in the low-frequency range and near the blade-passing frequency. The rotor–stator interaction is characterized by peak pressure pulsation energy at the blade-passing frequency and its harmonics. The spectrum reveals that the blade-passing frequency dominates the pressure pulsation spectrum at the impeller outlet, contributing the most energy and exhibiting a higher amplitude compared to its harmonics. The development of complex flow structures

appears to suppress the rotor–stator interaction, as indicated by the broad-frequency characteristics and reduced amplitude of the blade-passing frequency in the frequency-domain plot.

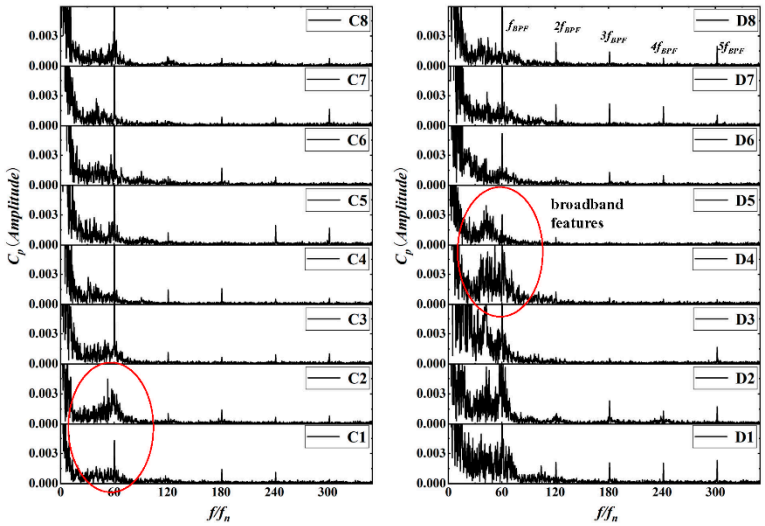


Figure 16. Frequency-domain characteristics of measuring points at the outlet of the wide impeller and narrow impeller under inlet condition 1.

Figure 17a,b illustrate the distribution of blade-passing frequency amplitude for pressure pulsations at various circumferential monitoring points at the impeller outlet. The superimposed amplitudes of the wide and narrow impellers at corresponding section monitoring points are shown in Figure 17c. Under inlet condition 1, the minimum superimposed BPF amplitude is 0.0018, while under inlet condition 2, it is 0.0038. For inlet condition 3, the minimum superimposed BPF amplitude reaches 0.009.

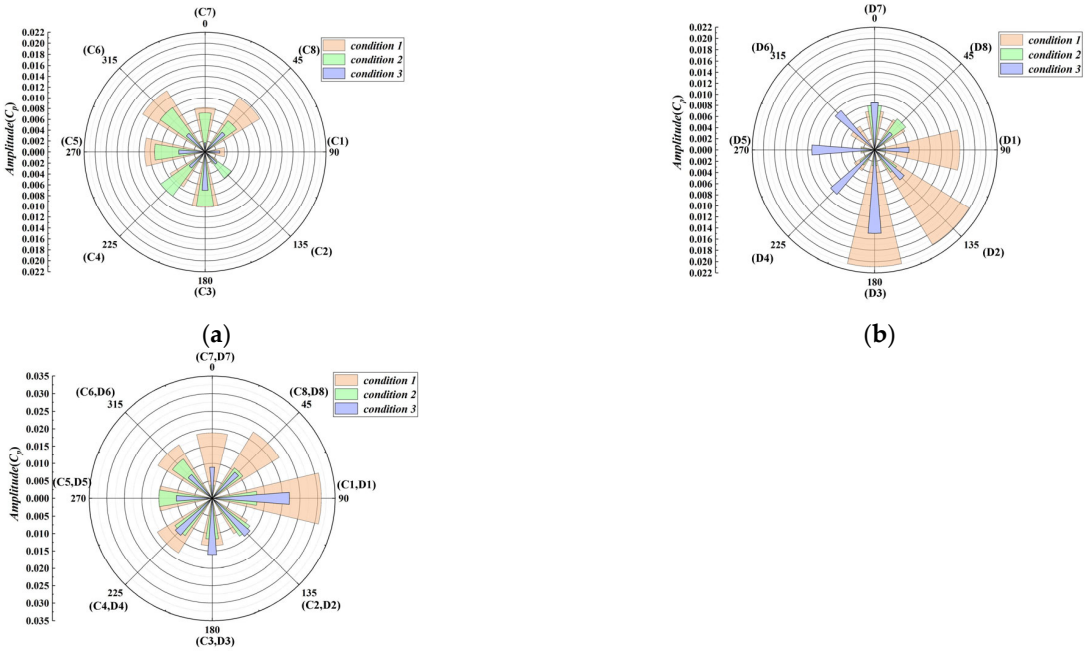


Figure 17. Circumferential distribution of C_p amplitude at blade-passing frequency (f_{BPF}). (**a**) From the wide impeller monitors. (**b**) From the narrow impeller monitors. (**c**) Superimposed values of measuring points on the same section.

Under inlet condition 1, the internal flow within the impeller is notably complex, leading to the highest amplitude of low-frequency broadband pulsations. This complex flow significantly reduces the BPF amplitude. Specifically, under this condition, the minimum BPF amplitude for the wide impeller is observed at monitoring point C2 (the fourth section), while for the narrow impeller, it is at monitoring point D5 (the seventh section). Under inlet condition 2, the minimum BPF amplitude for the wide impeller is at monitoring point C1 (the third section), and for the narrow impeller, it is at monitoring point D1 (the third section). For inlet condition 3, the minimum BPF amplitude for the wide impeller is recorded at monitoring point C7 (the first section), whereas for the narrow impeller, it is at monitoring point D8 (the second section).

3.4. Correlation Between Flow Structures and Pressure Pulsation

To investigate the relationship between pressure pulsation signals and unsteady flow structures within the fan, vortex structures in the impeller are identified using the Q-criterion. Developed by Hunt et al., the Q-criterion highlights areas of the flow field where the second invariant of the velocity gradient tensor reveals vortex structures. This criterion is expressed as follows:

$$Q = \frac{1}{2}\left(\|B\|_F^2 - \|A\|_F^2\right) \tag{8}$$

where A and B represent the symmetric and anti-symmetric matrices, respectively. $||\ ||_F$ denotes the Frobenius norm of the matrix.

Figure 18 shows that complex transient structures with high vortices appear near monitoring point C1 for the wide impeller section and near monitoring point D5 for the narrow impeller section. These two points correspond to the locations with the minimum amplitude of pressure pulsations at the blade-passing frequency (BPF). The reason for this is the inhibitory effect of the evolution of complex vortices on aerodynamic interference. The time interval Δt in the subsequent analysis is set to 0.0083 s (60°) to analyze the evolution process of internal impeller vortex structures within one rotation cycle.

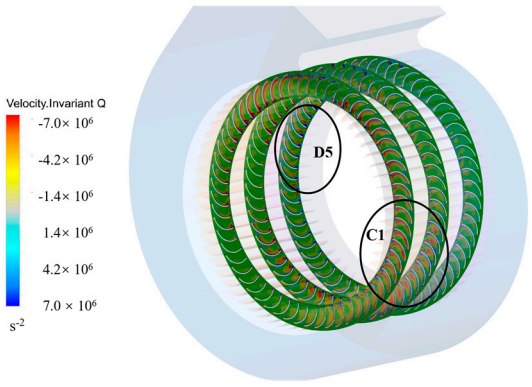
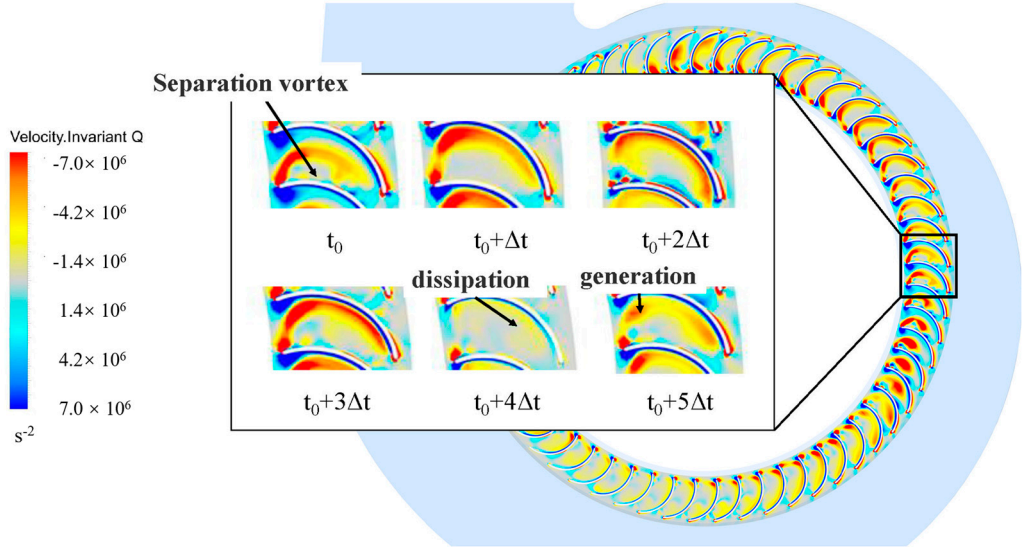


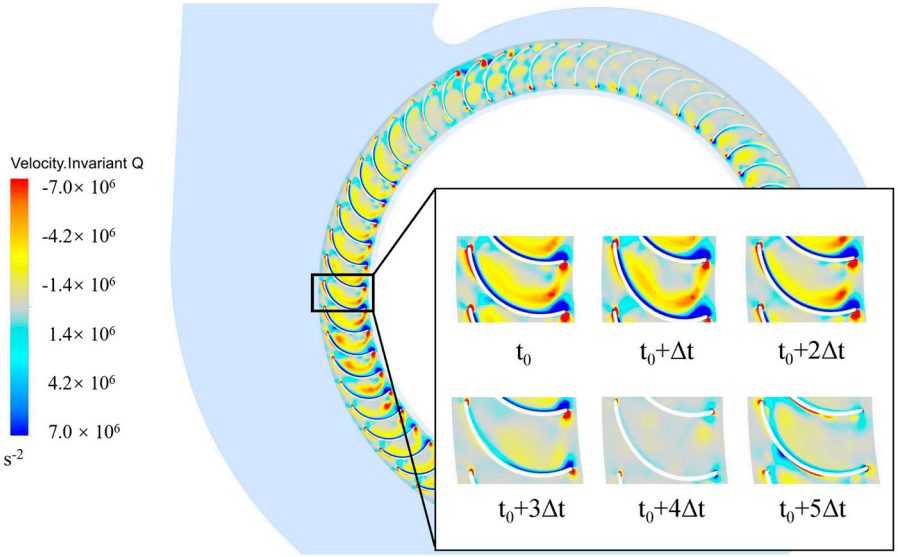
Figure 18. Vortex distribution of different axial sections.

Figure 19 illustrates that the high-vortex region near monitoring point C1 on the wide impeller originates from the blade's leading edge. The forward blade design positions negative vortices near the pressure side, while positive vortices emerge from the leading edge and merge with negative vortices near the pressure side of the adjacent blade. This interaction results in the shedding of large-scale vortices on the pressure side, while smaller-scale separation vortices predominantly shed on the suction side. At time t_0, the large-scale vortices peak in intensity, nearly filling the entire impeller passage. By time t0 + Δt, these vortices impact the pressure side, breaking up and dissipating within the passage. At time t0 + 5Δt, regeneration of the large-scale vortices begins. Throughout this cycle, the intensity

of the smaller separation vortices remains largely unaffected, which primarily influences the amplitude of the blade-passing frequency (BPF) due to the large-scale vortices. In contrast, near monitoring point D5 on the narrow impeller, the transient vortex structure lacks smaller separation vortices. Only a pair of large-scale vortices is observed, with weaker vortex energy and a reduced impact on the BPF signal.



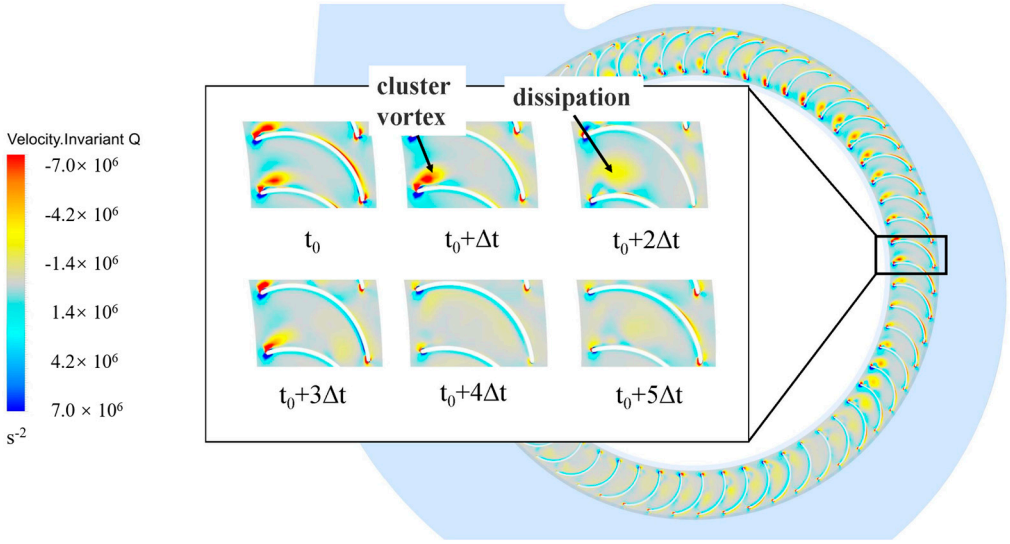
(**a**) Wide impeller



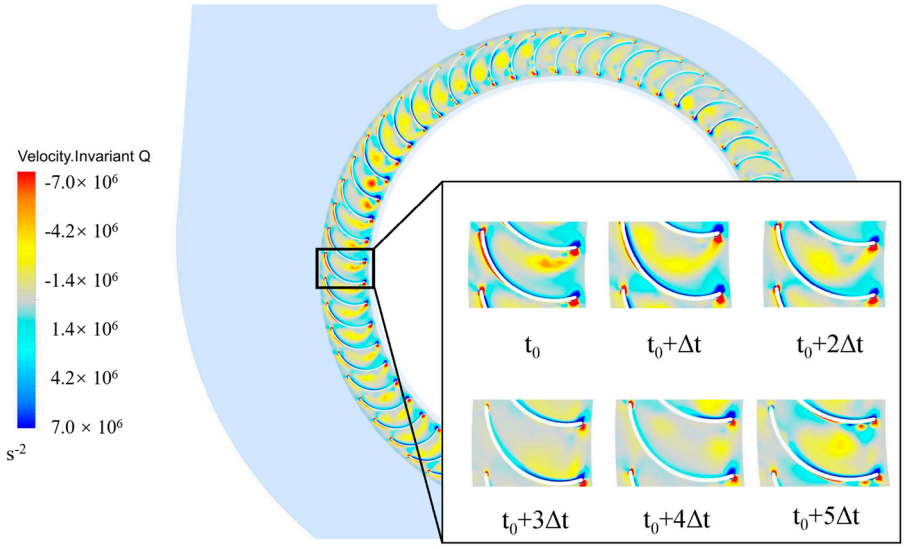
(**b**) Narrow impeller

Figure 19. Flow structure transient evolution in the flow passage of inlet condition 1.

In Figure 20, under inlet condition 2, the overall vortex strength is significantly reduced compared to inlet condition 1. The vortex structure within the wide blade passage shifts from a striped pattern to a predominantly clustered formation. Throughout a single rotation cycle, the vortex originates from the leading edge at time t_0 and gradually fragments as it progresses towards the trailing edge, eventually forming an isolated positive vortex cluster that persists within the passage. By time t0 + 4Δt, the strength of this vortex cluster reaches its minimum before regenerating from the leading edge in the next time step. In contrast, the transient vortex structure within the narrow blade passage maintains its striped pattern, as the high-energy vortex clusters generated at the leading edge do not undergo fragmentation.



(**a**) Wide impeller



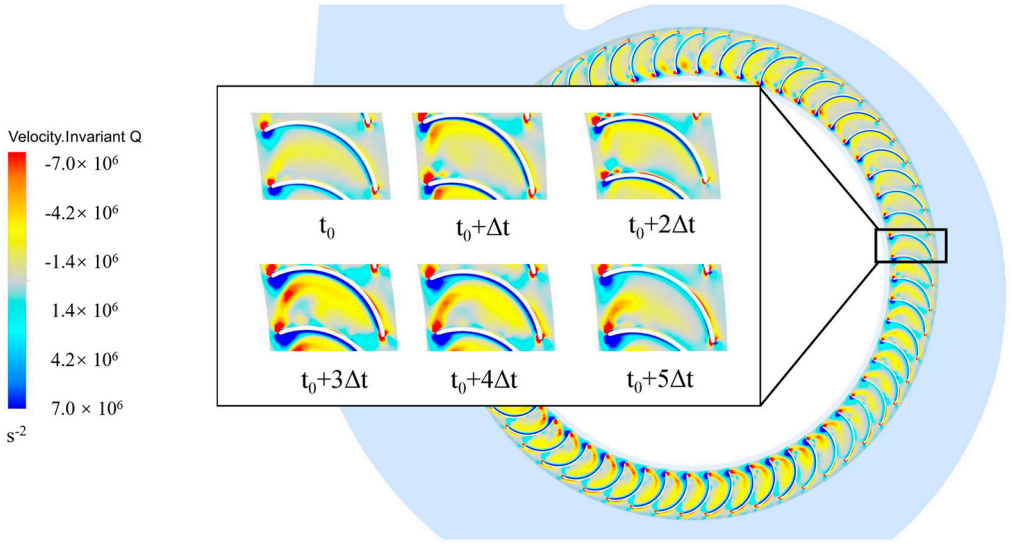
(**b**) Narrow impeller

Figure 20. Flow structure transient evolution in the flow passage of inlet condition 2.

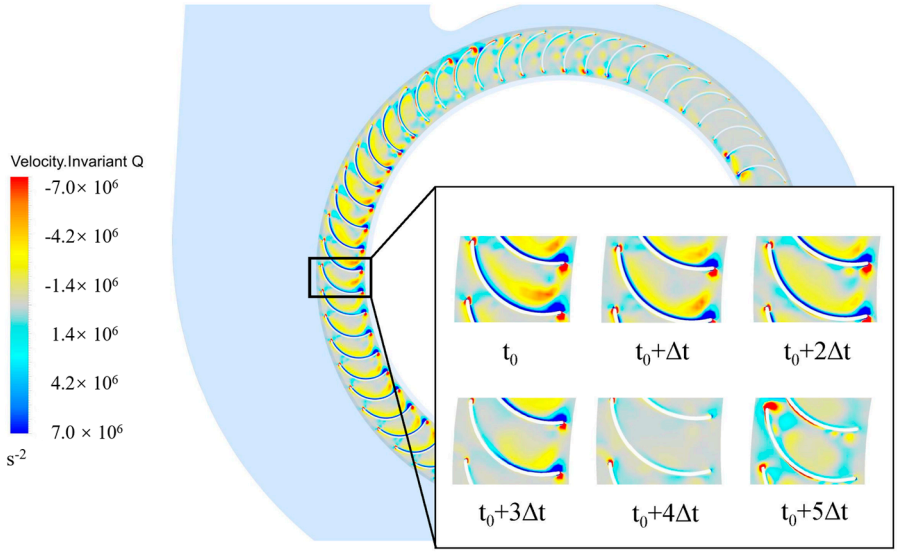
Figure 21 demonstrates that under inlet condition 3, vortex shedding within both the wide and narrow blade passages exhibits a striped pattern. The vortex structures maintain consistent strength and distribution throughout the passages, both spatially and temporally. This inlet condition achieves an optimal internal flow state for the impeller, characterized by a pronounced dynamic–static interference effect. Furthermore, there are no significant broad-frequency signals detected near the blade-passing frequency.

Under non-uniform inlet conditions, the flow at the impeller inlet is complex, featuring significant variations in both velocity and direction. These fluctuations result in unbalanced aerodynamic forces acting on the blades during rotation, leading to pressure fluctuations at the impeller outlet. For instance, when the left inlet serves as the primary air source, the left blades experience greater impact forces during rotation, which causes more pronounced pressure fluctuations on the left side of the impeller outlet. This observation aligns with the higher amplitude of low-frequency and broadband fluctuations noted near the monitoring points on the left side, as illustrated in Figures 19–21. The asymmetric vortex structures also influence the pressure distribution. As demonstrated in Figure 21, the vortex structures within both the wide and narrow impellers display a striped distribution.

The consistent strength and arrangement of these vortices contribute to relatively stable pressure fluctuations at the impeller outlet, characterized by a smaller amplitude of the pressure coefficient.



(**a**) Wide impeller



(**b**) Narrow impeller

Figure 21. Flow structure transient evolution in the flow passage of inlet condition 3.

4. Sound Quality

The acoustic field test was carried out in a simulated kitchen laboratory, with the experimental platform arranged as shown in Figure 22. The kitchen floor, walls, and ceiling were constructed from smooth, reflective materials such as concrete, metal, or ceramic tiles. To reduce interference with the sound source during testing, only one operator was allowed in the lab, and they were required to avoid wearing clothing with significant sound-absorbing properties that could impact the results. To evaluate human perception of noise, dummy heads (depicted in Figure 23) were placed at measurement points to capture data on how personnel in front of the stove perceive fan noise through the left and right ears of the artificial head.

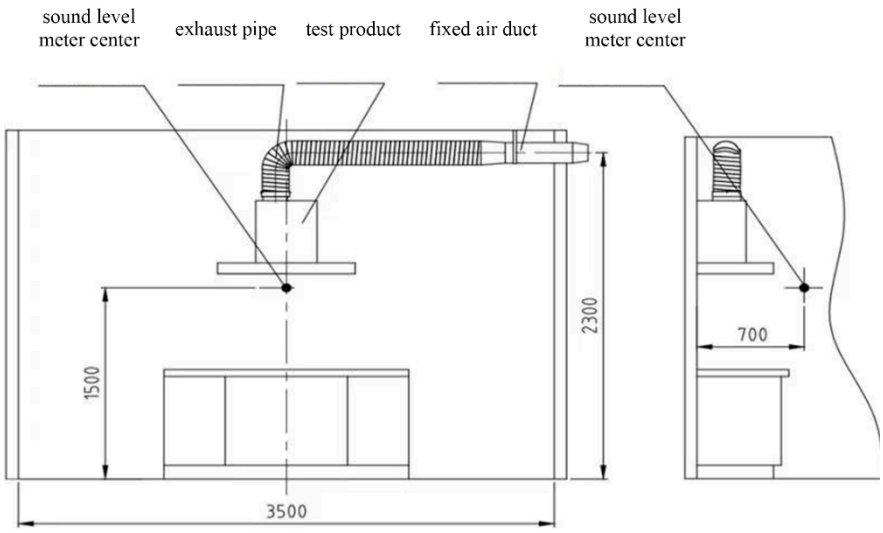


Figure 22. Layout diagram of the test bench.

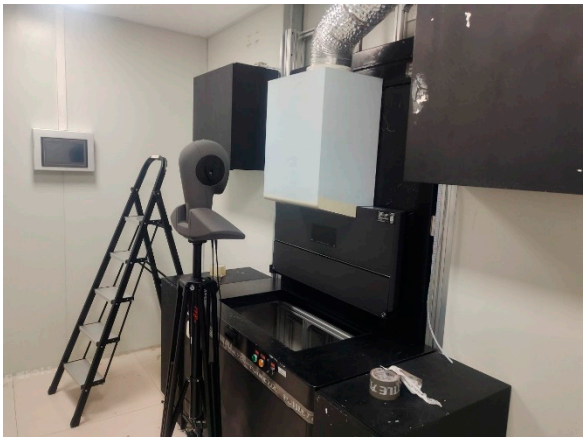


Figure 23. Artificial head schematic diagram.

The process of collecting sound signals and developing models involves several key steps: gathering sound samples from range hoods, objectively evaluating the samples' parameters, subjectively assessing the samples, performing statistical analysis, and creating models. Initially, the loudness (L), sharpness (S), roughness (R), and articulation index (AI) of the range hood sound samples are measured. The method for calculating these four parameters refers primarily to the standard TCAS 341-2019 [44], which outlines the test methods for noise and sound quality of range hoods. A selected group of participants then listens to these samples under controlled conditions to ensure accurate representation, providing subjective comfort ratings for the sound quality. A regression model is then established to correlate the objective parameters with the subjective comfort ratings, leading to a final calculation formula for sound quality comfort Q.

$$Q = 10.7067 - 0.026 \times L - 0.5 \times S - 2.4298 \times R + 3.1657 \times AI \quad (9)$$

Loudness quantifies how the human ear perceives the overall volume of sound, measured in sones. For reference, the loudness of a pure 1 kHz tone at a sound pressure level of 40 dB is defined as 1 sone. The second row of Figure 19 displays the variations in loudness over time, recorded from the left and right ears of an artificial head. The data reveal from Figure 24 that under inlet condition 1, the left ear perceives a loudness of 26.6 sones, while the right ear perceives 28 sones. Under inlet condition 2, the average

loudness decreases to 24.2 sones in the left ear and 25.2 sones in the right ear. Inlet condition 3 further reduces loudness to 21.8 sones in the left ear and 22.7 sones in the right. The highest loudness, observed under inlet condition 1, indicates that the fan's internal noise is most intense under this condition.

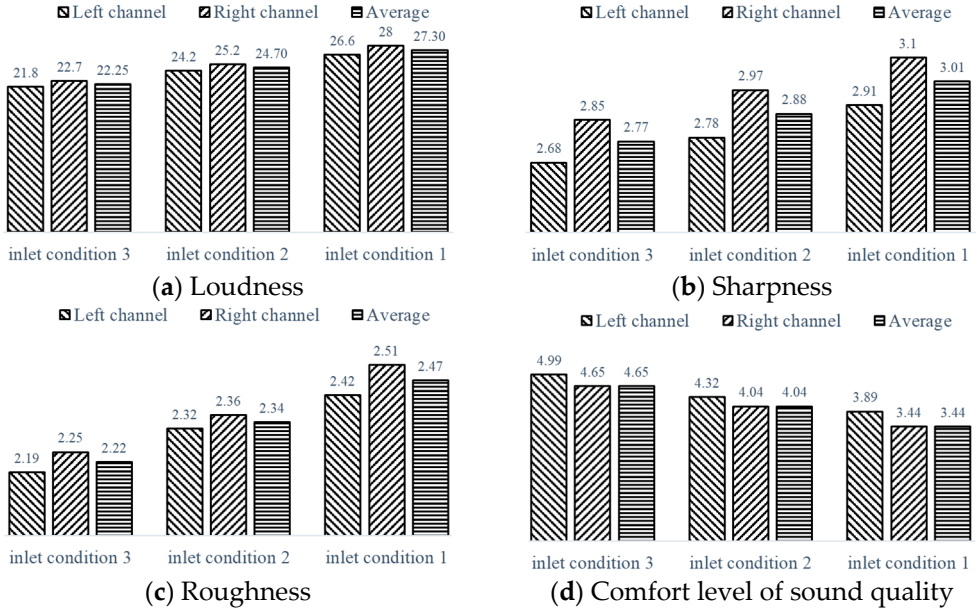
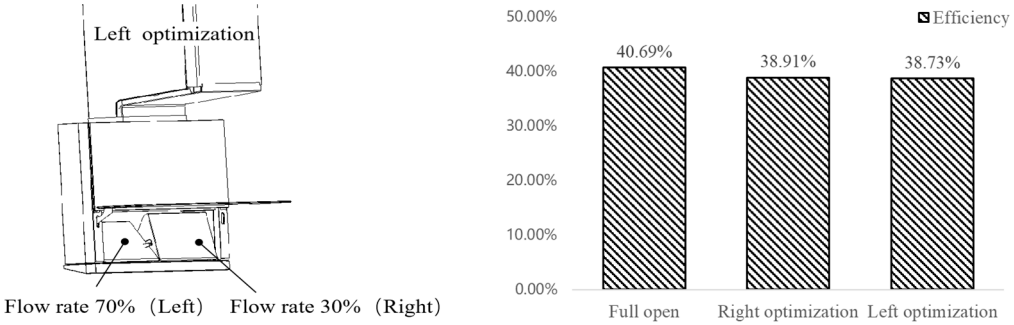


Figure 24. Comparison of sound quality parameters under three different intake conditions.

Sharpness is a psychoacoustic measure that evaluates the presence of high-frequency components in sound, expressed in acum. The third row of figures shows that sharpness is highest under inlet condition 1, with values of 2.91 acum in the left ear and 3.1 acum in the right ear. This suggests a higher concentration of high-frequency signals in the sound, corresponding to the broadband pulsation signal near the mid-frequency of the pressure pulsation, and is associated with the periodic evolution of large-scale vortices in the impeller flow passage.

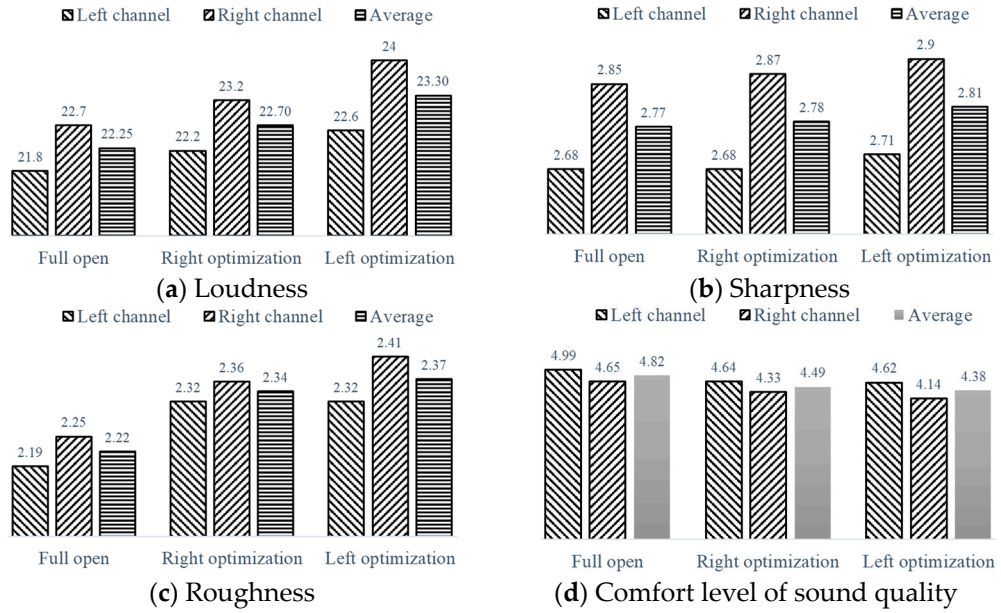
Sharpness of sound is a psychological measure used to assess the amount of high-frequency signal components in sound, and it is measured in acum. The data can be seen in the third row of the figures. Under inlet condition 1, the sharpness in the left and right ears is the highest, at 2.91 acum and 3.1 acum, respectively. Thus, it can be seen that under this inlet condition, the high-frequency signal in the sound is relatively high, corresponding to the wideband pulsation signal near the mid-frequency of the pressure pulsation, manifested as the periodic evolution of a pair of large-scale vortices in the impeller flow passage.

Based on inlet condition 1, a new inlet scheme with a non-uniform air volume distribution has been proposed to enhance aerodynamic performance and noise quality while preventing uneven oil fume escape. This scheme involves adjusting the angle of the guide plate at the intake structure, where the left side is fully opened and the right side is partially opened, resulting in an airflow ratio of 7:3. Alternatively, when the right side is fully opened and the left side is partially opened, the airflow ratio becomes 3:7. This approach aims to ensure that airflow is distributed evenly across the entire intake surface. Details of this optimization can be found in Figure 25. Figure 26 illustrates that, following the implementation of this optimization scheme, the aerodynamic performance parameters, including the maximum total pressure efficiency under the three intake conditions, remain consistent, with the maximum deviation in total pressure efficiency not exceeding 1.96%.



(**a**) Non-uniform inlet condition scheme (**b**) Maximum total pressure efficiency

Figure 25. The non-uniform inlet condition scheme and maximum total pressure efficiency.



(**a**) Loudness (**b**) Sharpness

(**c**) Roughness (**d**) Comfort level of sound quality

Figure 26. Comparison of sound quality parameters of optimization.

Figure 26 demonstrates that the optimization scheme effectively reduces the differences in loudness, sharpness, and roughness between the left and right ears. Specifically, the left-side optimization reduces the average loudness by four sones. Both optimization schemes achieve a deviation from the average loudness under fully open conditions of no more than 0.3 sones, sharpness by no more than 0.3 acum, and roughness by no more than 0.15 asper. These results suggest that the distribution characteristics of the internal vortex are consistent across the optimized conditions.

5. Conclusions

This study utilizes numerical simulations to explore how various inlet conditions influence the internal flow field and pressure pulsation of a dual-inlet centrifugal fan. The key findings are as follows:

(1) Time-domain analysis indicates that inlet condition 1 is the most unstable. This instability is characterized by significant fluctuations in the pressure coefficient and the presence of broadband signals in the frequency domain. These broadband features are particularly pronounced at measurement point C1, located on the wide impeller, and measurement point D5, located on the narrow impeller.

(2) Analysis of transient vortex structures reveals that the observed broadband characteristics and the absence of the blade-passing frequency at these measurement points are associated with the periodic evolution of large-scale vortices within the flow passage.

Under inlet condition 1, the intensity of the vortex peaks is due to the alignment between the inlet direction and the impeller's rotation direction, which has a substantial impact on flow within the passage.

(3) Sound quality analysis shows that under inlet condition 1, the sound sharpness is greater than under the other conditions. This observation suggests a higher presence of high-frequency signals in the pressure pulsation near the blade-passing frequency, further linking the flow structures to the characteristics in the frequency domain.

(4) A non-uniform air volume distribution scheme is proposed. This scheme enhances aerodynamic performance and reduces noise discrepancies between the left and right sides, leading to an overall reduction in average loudness by four sones.

Author Contributions: Conceptualization, Y.H.; methodology, Y.H. and Q.X.; software, Y.H. and B.L.; validation, W.Y., H.C. and J.W.; formal analysis, Y.H.; investigation, Y.H. and B.L.; resources, Y.H.; data curation, Q.X.; writing—original draft preparation, Y.H.; writing—review and editing, Y.H.; visualization, Y.H.; supervision, J.W. and Q.X.; project administration, W.Y. and Q.X.; funding acquisition, Y.H. All authors have read and agreed to the published version of the manuscript.

Funding: This research was supported by the National Key Research and Development Program of China (2023YFC3708405), the Open Research Fund of Science and Technology Innovation Platform of Key Laboratory of Renewable Energy Electric-Technology of Hunan Province, Changsha University of Science & Technology (2024ZNDL005).

Data Availability Statement: Data are contained within the article.

Acknowledgments: The authors thank the SCTS/CGCL HPCC of HUST for providing computing resources and technical support. The authors also appreciate Ningbo Fotile Kitchenware Co., Ltd. for their advice and assistance in improving this article.

Conflicts of Interest: Author Bin Li, Haohui Chen and Weigang Yang were employed by the company Ningbo Fotile Kitchenware Co., Ltd. The remaining authors declare that the research was conducted in the absence of any commercial or financial relationships that could be construed as a potential conflict of interest.

References

1. Darvish, M.; Frank, S.; Paschereit, C.O. Numerical and experimental study on the tonal noise generation of a radial fan. *J. Turbomach.* **2015**, *137*, 101005. [CrossRef]
2. Akbari, G.; Montazerin, N.; Akbarizadeh, M. Stereoscopic particle image velocimetry of the flow field in the rotor exit region of a forward-blade centrifugal turbomachine. *Proc. Inst. Mech. Eng. Part A J. Power Energy* **2012**, *226*, 163–181. [CrossRef]
3. Pretzsch, A.; Seidler, A.; Hegewald, J. Health Effects of Occupational Noise. *Curr. Pollut. Rep.* **2021**, *7*, 344–358. [CrossRef]
4. Bolm-Audorff, U.; Hegewald, J.; Pretzsch, A.; Freiberg, A.; Nienhaus, A.; Seidler, A. Occupational Noise and Hypertension Risk: A Systematic Review and Meta-Analysis. *Int. J. Environ. Res. Public Health* **2020**, *17*, 6281. [CrossRef]
5. Wen, X.; Mao, Y.; Yang, X.; Qi, D. Design Method for the Volute Profile of a Squirrel Cage Fan with Space Limitation. *J. Turbomach.* **2016**, *138*, 081001. [CrossRef]
6. Wang, K.; Ju, Y.; Zhang, C. Numerical investigation on flow mechanisms of a squirrel cage fan. *Proc. Inst. Mech. Eng. Part A J. Power Energy* **2019**, *233*, 3–16. [CrossRef]
7. Cho, G.R.; Kawahashi, M.; Hirahara, H.; Kitadume, M. Application of Stereoscopic Particle Image Velocimetry to Experimental Analysis of Flow through Multiblade Fan. *JSME Int. J. Ser. B* **2005**, *48*, 25–33. [CrossRef]
8. Wang, C.; Wang, M.; Mai, K.; Li, H.; Liu, N. Structure design of low-frequency broadband sound-absorbing volute for a multi-blade centrifugal fan. *Appl. Acoust.* **2020**, *165*, 107315. [CrossRef]
9. Benchikh Le Hocine, A.E.; Poncet, S.; Fellouah, H. CFD modeling and optimization by metamodels of a squirrel cage fan using OpenFoam and Dakota: Ventilation applications. *Build. Environ.* **2021**, *205*, 108145. [CrossRef]
10. Xiong, J.; Tang, J.; Guo, P.; Li, J. Flow Capacity Optimization of a Squirrel Cage Fan with a New Rounded Rectangle Volute under Size Limitation. *Machines* **2023**, *11*, 283. [CrossRef]
11. Wang, K.; Ju, Y.; Zhang, C. Aerodynamic optimization of forward-curved blade centrifugal fan characterized by inclining bionic volute tongue. *Struct. Multidiscip. Optim.* **2021**, *63*, 2493–2507. [CrossRef]

12. Kirchhofer, M.; Krieger, M.; Hofer, D. A Comparative Study on Numerical Flow Simulations of a Centrifugal Electronic Cooling Fan Using Four Different Turbulence Models. *Energies* **2023**, *16*, 7864. [CrossRef]
13. Yang, X.; Jiang, B.; Wang, J.; Huang, Y.; Yang, W.; Yuan, K.; Shi, X. Multi-objective optimization of dual-arc blades in a squirrel-cage fan using modified non-dominated sorting genetic algorithm. *Proc. Inst. Mech. Eng. Part A J. Power Energy* **2020**, *234*, 1053–1068. [CrossRef]
14. Ballesteros-Tajadura, R.; Velarde-Suárez, S.; Hurtado-Cruz, J.P.; Santolaria-Morros, C. Numerical Calculation of Pressure Fluctuations in the Volute of a Centrifugal Fan. *J. Fluids Eng.* **2005**, *128*, 359–369. [CrossRef]
15. Li, Z.; Cao, W.; Ye, X.; Wei, Y. Experimental Investigation on the Noise Characteristics of a Squirrel-Cage Fan with Different Blade Lengths. *Energies* **2022**, *16*, 69. [CrossRef]
16. Xu, L.; Hansen, A.C.; Li, Y.; Liang, Z.; Yu, L. Numerical and Experimental Analysis of Airflow in a Multi-Duct Cleaning System for a Rice Combine Harvester. *Trans. ASABE* **2016**, *59*, 1101–1110.
17. Zhang, H.; Yang, J.; Li, B.; Xia, C.; Zhang, Y. Noise reduction and aerodynamic performance improvement of a multiblade centrifugal fan. *Phys. Fluids* **2024**, *36*, 125168. [CrossRef]
18. Min, Y.H.; Kang, S.; Hur, N.; Lee, C.; Park, J. Performance assessment of the RANS turbulence models in prediction of aerodynamic noise for air—Conditioner indoor unit. *J. Comput. Fluids Eng.* **2012**, *17*, 81–86. [CrossRef]
19. Zhang, J.; Chu, W.; Zhang, J. Numerical study of volute casing vibro-acoustics in a marine centrifugal fan. *Aust. J. Mech. Eng.* **2021**, *19*, 502–520. [CrossRef]
20. Xiao, Q.; Wang, J.; Yang, X.; Ding, Y.; Jiang, B. An Empirical noise model of centrifugal fans with different volute tongues based on Langevin regression. *J. Build. Eng.* **2023**, *79*, 107876. [CrossRef]
21. Velarde-Suárez, S.; Ballesteros-Tajadura, R.; Santolaria-Morros, C.; González-Pérez, J. Unsteady Flow Pattern Characteristics Downstream of a Forward-Curved Blades Centrifugal Fan. *J. Fluids Eng.* **2001**, *123*, 265–270. [CrossRef]
22. Velarde-Suárez, S.; Ballesteros-Tajadura, R.; Pérez, J.G.; Pereiras-García, B. Relationship between volute pressure fluctuation pattern and tonal noise generation in a squirrel-cage fan. *Appl. Acoust.* **2009**, *70*, 1384–1392. [CrossRef]
23. Oro, J.M.; García, J.; Parrondo, J. Numerical investigation of the unsteady flow in a centrifugal fan: Impeller-tongue interaction. *J. Fluids Eng.* **2010**, *132*, 051102.
24. Oro, J.M.; García, J.; Parrondo, J. Experimental validation of numerical simulations of unsteady flow in a centrifugal fan. *Exp. Therm. Fluid Sci.* **2011**, *35*, 1–10.
25. Oro, J.M.; García, J.; Parrondo, J. Optimization of impeller-tongue interaction in centrifugal fans using CFD. *J. Turbomach.* **2014**, *136*, 031001.
26. Kato, C.; Kaiho, M.; Manabe, A. An Overset Finite-Element Large-Eddy Simulation Method With Applications to Turbomachinery and Aeroacoustics. *J. Appl. Mech.* **2003**, *70*, 32–43. [CrossRef]
27. Liu, E.; Yan, S.; Peng, S.; Huang, L.; Jiang, Y. Noise silencing technology for manifold flow noise based on ANSYS fluent. *J. Nat. Gas Sci. Eng.* **2016**, *29*, 322–328. [CrossRef]
28. Deng, X. A unified framework for non-linear reconstruction schemes in a compact stencil. Part 1: Beyond second order. *J. Comput. Phys.* **2023**, *481*, 112052. [CrossRef]
29. Deng, X. A new open-source library based on novel high-resolution structure-preserving convection schemes. *J. Comput. Sci.* **2023**, *74*, 102150. [CrossRef]
30. Cheng, L.; Deng, X.; Xie, B. An accurate and practical numerical solver for simulations of shock, vortices and turbulence interaction problems. *Acta Astronaut.* **2023**, *210*, 1–13. [CrossRef]
31. Gholamian, M.; Rao, G.K.M.; Bhramara, P. Numerical investigation on effect of inlet nozzle size on efficiency and flow pattern in squirrel cage fans. *Proc. Inst. Mech. Eng. Part A J. Power Energy* **2013**, *227*, 896–907. [CrossRef]
32. Huang, J.; Zhang, K.; Li, H.; Wang, A.; Yang, M. Numerical simulation of aerodynamic noise and noise reduction of range hood. *Appl. Acoust.* **2021**, *175*, 107806. [CrossRef]
33. Lv, H.; Yang, W.; Zhang, W.J. Numerical simulation and analysis of the aerodynamic noise of a nautilus-inspired bionic multiblade centrifugal fan. *J. Mech. Sci. Technol.* **2022**, *36*, 4475–4489. [CrossRef]
34. Lei, J.; Jia, C.; Cui, Q.; Cheng, W.; Qin, G. Cause analysis and suppression method of the vortex at the impeller outlet of the multiblade centrifugal fan. *Energy Sci. Amp; Eng.* **2023**, *11*, 3364–3378. [CrossRef]
35. Liu, H.; Jiang, B.; Wang, J.; Yang, X.; Xiao, Q. Numerical and experimental investigations on non-axisymmetric D-type inlet nozzle for a squirrel-cage fan. *Eng. Appl. Comput. Fluid Mech.* **2021**, *15*, 363–376. [CrossRef]
36. Jiang, B.; Wang, J.; Yang, X.; Wang, W.; Ding, Y. Tonal noise reduction by unevenly spaced blades in a forward-curved-blades centrifugal fan. *Appl. Acoust.* **2019**, *146*, 172–183. [CrossRef]
37. Xiao, Q.; Jang, B.; Wang, J. Volute profile design of the squirrel cage fan based on a B-spline curve under space limitation. *Proc. Inst. Mech. Eng. Part A J. Power Energy* **2020**, *234*, 889–899. [CrossRef]
38. Zhou, W.; Zhou, P.; Xiang, C.; Wang, Y.; Mou, J.; Cui, J. A Review of Bionic Structures in Control of Aerodynamic Noise of Centrifugal Fans. *Energies* **2023**, *16*, 4331. [CrossRef]

39. Yuan, Y.; Xiao, Y.; Ming, P.; Lu, H. The aerodynamic and noise characteristics of centrifugal fan with partially tilted tongue. *Phys. Fluids* **2023**, *35*, 127113. [CrossRef]
40. Paramasivam, K.; Rajoo, S.; Romagnoli, A.; Yahya, W.J. Tonal noise prediction in a small high speed centrifugal fan and experimental validation. *Appl. Acoust.* **2017**, *125*, 59–70. [CrossRef]
41. Zhang, A.T.; Zhou, B.S.; Mao, C.Z.; He, D.J.; Fang, E.X. A design method of volute profile of multi-blade centrifugal fan based on DRBF model. *Phys. Fluids* **2023**, *35*, 125127. [CrossRef]
42. Wang, J.; Liu, X.; Tian, C.; Xi, G. Aerodynamic performance improvement and noise control for the multi-blade centrifugal fan by using bio-inspired blades. *Energy* **2023**, *263*, 125829. [CrossRef]
43. Zhou, S.; Zhou, H.; Yang, K.; Dong, H.; Gao, Z. Research on blade design method of squirrel-cage fan for building efficient ventilation based on Hicks-Henne function. *Sustain. Energy Technol. Assess.* **2021**, *43*, 100971.
44. *T/CAS 341-2019*; Test Method for Sound Quality of Range Hood Noise. Chinese Group Standards: Beijing, China, 2019.

Disclaimer/Publisher's Note: The statements, opinions and data contained in all publications are solely those of the individual author(s) and contributor(s) and not of MDPI and/or the editor(s). MDPI and/or the editor(s) disclaim responsibility for any injury to people or property resulting from any ideas, methods, instructions or products referred to in the content.